ACS APPLIED MATERIALS & INTERFACES

Research Article

www.acsami.org

Perfluoropentane-Encapsulated Hollow Mesoporous Prussian Blue Nanocubes for Activated Ultrasound Imaging and Photothermal Therapy of Cancer

Xiaoqing Jia,[†,‡,⊥] Xiaojun Cai,[†,⊥] Yu Chen,[†] Shige Wang,[†] Huixiong Xu,[§] Kun Zhang,[†] Ming Ma,[†] Huixia Wu,[*,‡] Jianlin Shi,[†] and Hangrong Chen[*,†]

[†]State Key Laboratory of High Performance Ceramics and Superfine Microstructure, Shanghai Institute of Ceramics, Chinese Academy of Sciences, 1295 Ding-xi Road, Shanghai, 200050, China

[‡]The Key Laboratory of Resource Chemistry of Ministry of Education and the Shanghai Key Laboratory of the Rare Earth Functional Materials, Department of Chemistry, College of Life and Environmental Science, Shanghai Normal University, Shanghai 200234, P. R. China

[§]Tenth Peoples Hospital of Tongji University, Shanghai 200072, P. R. China

Supporting Information

ABSTRACT: Hollow mesoporous nanomaterials have gained tremendous attention in the fields of nanomedicine and nanobiotechnology. Herein, *n*-perfluoropentane (PFP)-encapsulated hollow mesoporous Prussian blue (HPB) nanocubes (HPB-PFP) with excellent colloidal stability have been synthesized for concurrent in vivo tumor diagnosis and regression. The HPB shell shows excellent photothermal conversion efficiency that can absorb near-infrared (NIR) laser light and convert it into heat. The generated heat can not only cause tumor ablation by raising the temperature of tumor tissue but also promote the continuous gasification and bubbling of encapsulated liquid PFP with low boiling point. These formed PFP bubbles can cause tissue impedance mismatch, thus apparently enhancing the signal of B-mode ultrasound imaging in vitro and generating an apparent echogenicity signal for tumor tissues of nude mice in vivo. Without showing observable in vitro and in vivo cytotoxicity, the designed biocompatible HPB-PFP nanotheranostics with high colloidal stability and photothermal efficiency are anticipated to find various biomedical applications in activated ultrasound imaging-guided tumor detection and therapy.

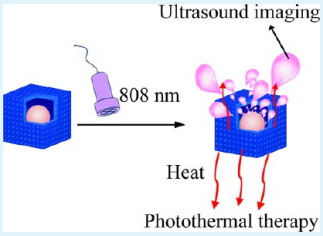

KEYWORDS: *ultrasound imaging, Prussian blue, photothermal therapy, n-perfluoropentane, cancer*

INTRODUCTION

With the development of material science and nanotechnology, nanoscale biomaterials have attracted ever-increasing attention in the early diagnosis and efficient therapy of cancer. Prussian blue (PB) has served as a blue dye for hundreds of years. Recently, various PB nanoparticles (NPs) have been prepared, and their corresponding properties[1−5] and potential applications as catalysts,[6−9] contrast agents,[4,10−12] drug and guest molecule carriers,[10,13] etc. have been investigated. In particular, the mutual transition between Fe^{2+} and Fe^{3+} provides PB NPs additional functions for oncology, such as ultrasound (US) imaging, magnetic resonance imaging, photoacoustic tomography, and photothermal therapy (PTT).[4,10−12,14]

Among the conventional tumor-therapeutic modalities, chemotherapy and radiotherapy are widely used clinical cancer treatment methods.[15] However, side-effects such as unavoidable injury to normal tissue greatly limit their cancer-therapeutic effects. PTT has been regarded as a less invasive but efficient tumor-therapeutic alternative that utilizes a photothermal conversion agent which can accumulate at tumor sites by either passive enhanced permeability and retention (EPR) effect or active targeting via the specific bonding between nanomaterials and tumor cells to absorb and convert near-infrared (NIR) laser light into heat to kill tumor cells.[14,16−20] For PTT, the key point is the design and fabrication of photothermal conversion agents with high biocompatibility and biosafety and high photothermal conversion efficiency. So far, several kinds of photothermal conversion agents have been explored, including various gold nanostructures (e.g., nanostars, nanocages, nanoshells, nanorods, bellflowers),[20−24] carbon nanomaterials (carbon nanotubes, graphene oxide, etc.),[25−31] copper chalcogenides,[32−37] defective tungsten oxide nanomaterials (nanorods, nanowires),[38−41] organic compounds (polypyrrole, polyaniline, and indocyanine green),[42−44] etc. Although tremendous investigations have been conducted to evaluate their therapeutic efficiency and biosafety both in vitro and in vivo, the intrinsic instability and potential toxicity have limited their further clinical translations. Because of the strong NIR light absorption and high photothermal conversion efficiency, PB NPs have been synthesized as a contrast agent

Received: October 28, 2014
Accepted: February 3, 2015
Published: February 3, 2015

DOI: 10.1021/am507443p
ACS Appl. Mater. Interfaces 2015, 7, 4579−4588

for enhanced photoacoustic tomography[11] and a photothermal conversion agent for PTT with photothermal stability.[14]

Benefiting from the features of noninvasiveness, excellent soft-tissue resolution, real-time imaging, high safety and convenience, US imaging has been widely accepted for clinical diagnosis.[45] Many kinds of organic microbubbles (such as denatured albumins, surfactants, or phospholipids shells) loaded with perfluorocarbon are clinically used as US contrast agents to increase the relative echogenicity and imaging sensitivity of deep tissues.[46−48] Some multifunctional micro- and nanosystems such as liposomes, aptamer-cross-linked microbubbles, poly(lactic-*co*-glycolic acid), porphyrin−phospholipid conjugates, Au nanocages, hollow mesoporous silica nanoparticles,[49−53] etc., have been designed and fabricated as novel kinds of US imaging contrast agents to enhance the ultrasound imaging sensitivity. However, the large particle size and poor stability severely limit their applications. As a kind of volatile liquid, the perfluorocarbon has been frequently applied clinically because of their FDA-approved biological safety (FDA, U.S. Food and Drug Administration) and easy excretion by reticuloendothelial system or pulmonary circulation. Upon the heat irradiation to surrounding tissues, perfluorocarbon could be readily vaporized and converted into a steamy state, which can result in high tissue impedance mismatch and US imaging enhancement. Thus, perfluorocarbon has been demonstrated as an excellent contrast agent for the enhanced ultrasound imaging.[54]

Although PB NPs have been studied for PTT,[14] and hollow mesoporous Prussian blue (HPB) NPs with defined mesoporous structure have been synthesized,[1] US-guided PTT by loading phase-change materials into the hollow interior of HPB NPs has not been found. Herein, *n*-perfluoropentane-encapsulated HPB NPs (HPB-PFP) have been designed and prepared for enhancing US imaging and efficient photothermal therapy of cancer both in vitro and in vivo. As shown in Scheme 1A, the mesoporous Prussian blue (mPB) nanocubes are etched by hydrochloric acid (HCl) to form HPB. mPB/HPB presents a cube structure, and the vibration of free electrons between Fe^{2+} and Fe^{3+}endows HPB with high photothermal conversion efficiency.[55] The large cavity structure makes it easy to encapsulate PFP by vacuum infusion (Scheme 1B). The heat produced by the photothermal transformation of HPB when irradiated by NIR laser light can not only cause the coagulation necrosis of tumor cells but also cause the liquid−gas phase change and bubble formation of PFP (low boiling point, 29 °C). The continuously emerging PFP bubbles can enhance the echogenicity and backscattering of the ultrasound, thus improving the sensitivity of US imaging. Therefore, the as-prepared HPB-PFP should be an excellent nanoplatform for real-time US imaging-guided PTT of cancer.

Scheme 1. (A) Schematic Illustration of the Preparation Process of HPB and Its Microstructure; (B) Schematic Illustration of HPB-PFP Formation and US-Guided PTT upon Laser Irradiation

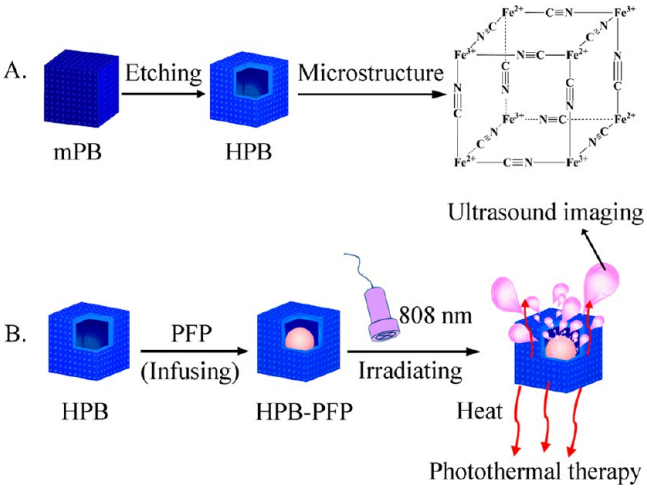

EXPERIMENTAL SECTION

Materials. Potassium hexacyanoferrate(III) ($K_3[Fe(CN)_6]$) (AR), poly(vinylpyrrolidone) (PVP, K30) (GR), and HCl were from Sinopharm Chemical Reagent Co., Ltd. Phosphate buffer solution (PBS), Dulbecco's modified eagle's medium (DMEM), and fetal bovine serum (FBS) were got from Gibco. All chemicals were used without further purification.

Characterization and Instrumentation. The structure and morphology of mPB and HPB were characterized by transmission electron microscopy (TEM, JEM-2100F), scanning electron microscopy (SEM, JSM-6700F), scanning transmission electron microscopy (STEM, FEI), and element mapping. ζ potentials and size distributions were measured by Malvern Nano ZS90 Zetasizer Nanoseries system. The infrared spectra were measured by Fourier transform infrared spectroscopy (FTIR, IS10 Nicolet, U.S.). The UV−vis−NIR absorption spectra curves were detected by UV−vis−NIR spectrophotometer (UV-3600 Shimadzu). Ultrasound imaging was performed with IU22 (Philips company).

Synthesis of HPB. For the synthesis of solid PB nanocubes, 132 mg of $K_3[Fe(CN)_6]$ and 3 g of PVP were dissolved in 0.01 M of HCl (40 mL) by stirring for 30 min at room temperature. The formed yellow solution was then heated in an electric oven of 80 °C. After 20 h, mPB NPs were collected by centrifugation and washed with distilled water. HPB NPs were obtained as follows: 20 mg of mPB and 200 mg PVP were mixed to 1 M of HCl solution (20 mL) in a Teflon vessel and stirred for 3 h. Then the vessel was sealed and reacted in an electric oven at 140 °C for 4 h. The HPB precipitates were collected by centrifugation and washed with distilled water. In the etching approach, some of the $K_3[Fe(CN)_6]$ will react with HCl and give birth to the toxic HCN; therefore, special attention should be given when handling the wastewater.

Synthesis of HPB-PFP. The HPB-PFP was prepared through a typical vacuum infusion method. The prior freeze-dried HPB (50 mg) was wrapped in a 5 mL bottle with a rubber plug and tightly covered with the parafilm. The bottle was evacuated by a syringe needle linked with a vacuum pump for 5 min. Then 150 μL of PFP was injected into the bottle and ultrasonicated in an ice−water bath for 2 min. PFP-encapsulated HPB was dispersed in 10 mL of PBS and stored at 4 °C for future use.

Photothermal Conversion Efficiency of HPB. First, different concentrations of HPB suspensions in PBS (12.5, 25, 50, 100, and 200 ppm) were prepared and their UV−vis−NIR absorption spectra were obtained by ultraviolet and visible spectrophotometery. HPB/HPB-PFP (1 mL, 400 ppm) suspensions were irradiated by 808 nm laser light at 2.5 W/cm^2. Then, 1 mL solutions of HPB (0, 25, 50, 100, and 200 ppm) in PBS in quartz cell were irradiated by 808 nm laser light at 2.5 W/cm^2 or 5 W/cm^2. The temperature changes of these solutions were recorded with a homemade temperature conductor.

In Vitro Cytocompatibility Evaluation. HeLa (human cervical cancer) cells were seeded into a 96-well plate with a density of 10^4 cells per well and cultured in an incubator with 5% CO_2 at 37 °C for 24 h. Then, 100 μL of HPB dispersion (0, 50, 100, 200, and 400 ppm, in DMEM) was added into the individual well. After 24 and 48 h, 100 μL of MTT (3-(4,5-dimethylthiazol-2-yl)-2,5-diphenyltetrazolium bromide) solution of 0.8 mg/mL was added and incubated for another 4 h. Then, 100 μL of DMSO was added into the plate to dissolve the MTT formazan. The plate was read at 490 nm using a Microplate

DOI: 10.1021/am507443p
ACS Appl. Mater. Interfaces 2015, 7, 4579−4588

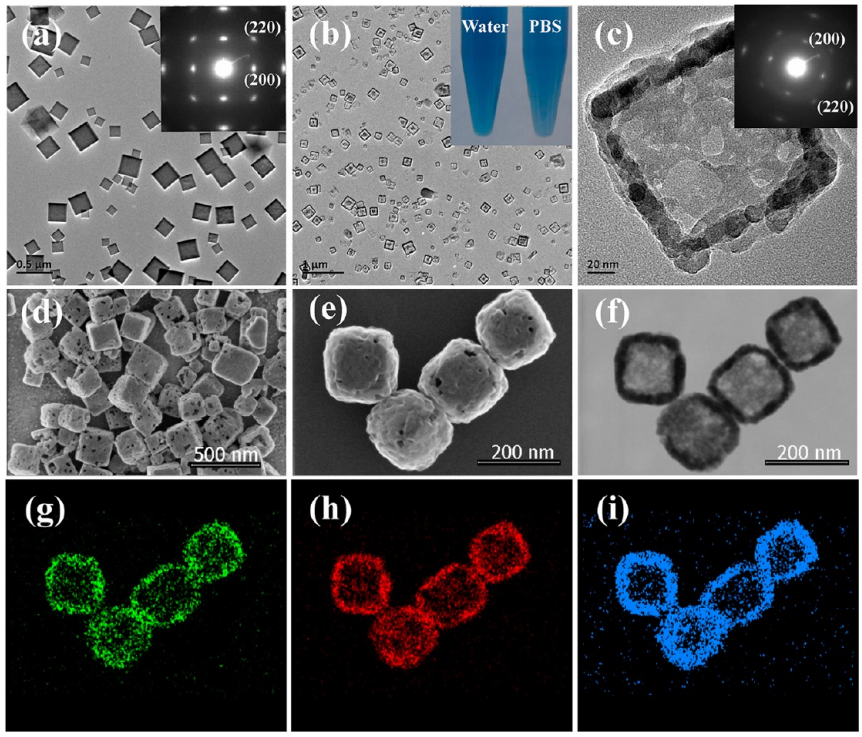

Figure 1. (a) TEM image of mPB; inset of (a), electron diffraction image of mPB. (b, c, f) TEM images of HPB; inset of (b), HPB suspensions in water and PBS; inset of (c), electron diffraction image of HPB. (d, e) SEM images of HPB with different magnifications. (f–h) Corresponding bright-field imaging and element mapping (g, N; h, Fe; i, C).

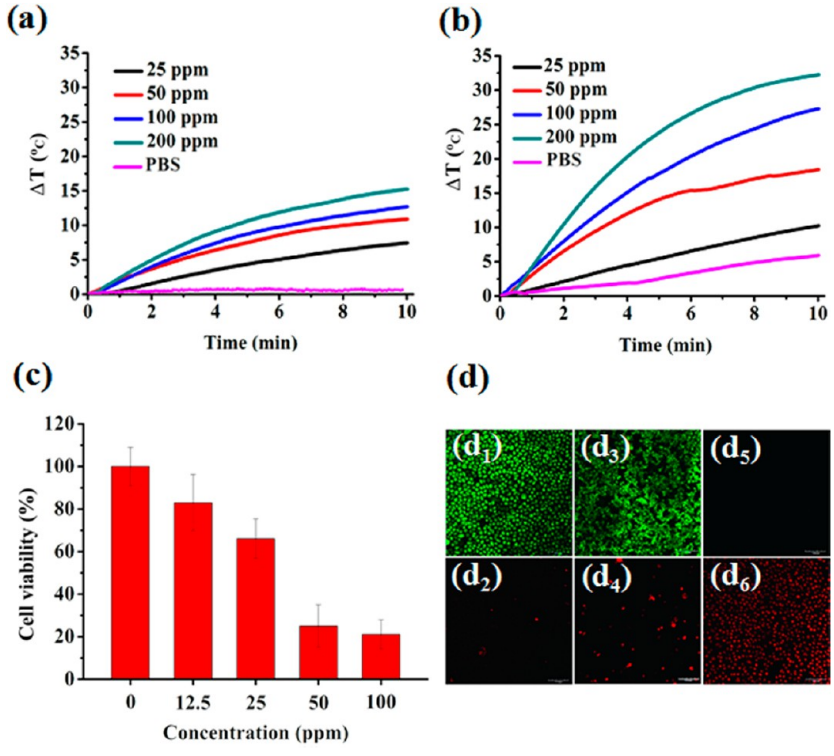

Figure 2. Evaluations of in vitro PTT efficiency. (a, b) Temperature-change curves of HPB solution under 808 nm laser irradiation (a, 2.5 W/cm^2; b, 5 W/cm^2; the initial temperature was room temperature of 22 °C). (c) HeLa cell viability after cocultured with HPB at different concentrations (0, 12.5, 25, 50, 100 ppm) and irradiated by 808 nm laser light (5 W/cm^2, 5 min). (d) CLSM images of HeLa cells after cocultured with HPB suspension (50 ppm) and irradiated by 808 nm laser light at 5 W/cm^2 (d_1 and d_2, control; d_3 and d_4, 5 min; d_5 and d_6, 10 min; d_1, d_3, and d_5, the calcein channel; d_2, d_4 and d_6, the PI channel).

Reader (Biotek, U.S.). Mean and standard deviations for the triplicate wells for each sample were reported.

In Vitro Photothermal Effect. For the in vitro PTT, HeLa cells with a density of 10^4 cells per well were seeded into a 96-well plate in

DOI: 10.1021/am507443p
ACS Appl. Mater. Interfaces 2015, 7, 4579–4588

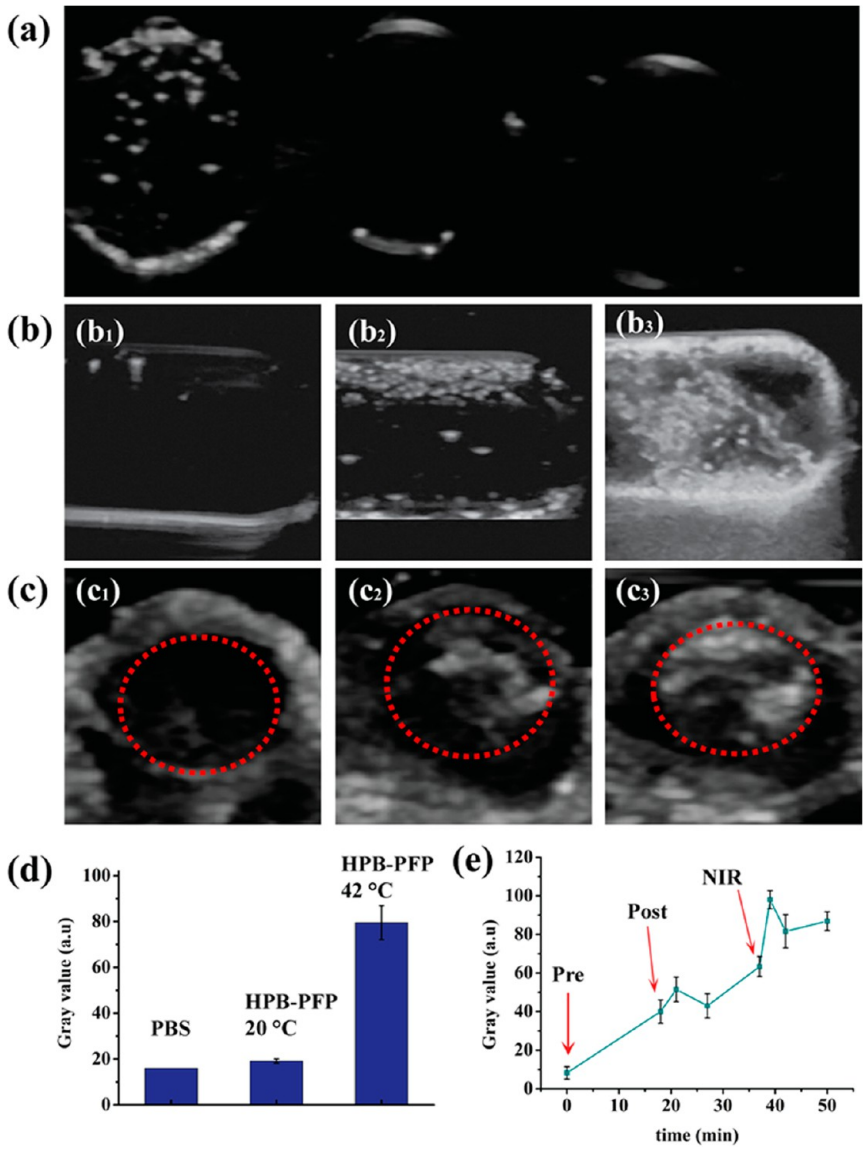

Figure 3. In vitro and in vivo US imaging results. (a) US images of HPB-PFP/HPB/PBS at 42 °C (left, HPB-PFP (100 ppm); middle, HPB (100 ppm); right, PBS). (b) b_1, PBS at 20 °C; b_2, HPB-PFP solution at 20 °C; b_3, HPB-PFP solution at 42 °C. (c) In vivo US images of tumor site (red dotted circle) (c_1) before and (c_2) after injection of HPB-PFP solution (30 μL, 200 ppm) and (c_3) after being irradiated by 808 nm laser light at 2 W/cm^2 for 5 min. (d) Gray values of in vitro US imaging corresponding to those in panel b. (e) Gray values of in vivo US imaging corresponding to those in panel c, for a duration of 50 min from preinjection.

100 μL of DMEM overnight. The medium was replaced by fresh medium containing HPB (0, 12.5, 25, 50, and 100 ppm). After incubation for 4 h, the cells were exposed under the 808 nm NIR laser light for 5 min at a power density of 5 W/cm^2 and then back incubated for another 20 h. The cell metabolic activity was quantified using MTT assay asmentioned above.

Confocal laser scanning microscope (CLSM) was further used to qualitatively evaluate the in vitro photothermal effect of HPB. HeLa cells were seeded into a confocal dish with a density of 10^5 per dish and cultured at 37 °C for 24 h. Then, 1 mL of fresh DMEM containing HPB (50 ppm) was added. After the cells were cultured 4 h, the cells were irradiated by the 808 nm laser light at 5 W/cm^2 for 5 or 10 min. Untreated cells were set as control. Then, all cells were dyed with calcein and PI and observed with CLSM.

In Vitro Ultrasound Imaging of HPB-PFP. The solution of PBS (control) or HPB-PFP (200 ppm, 3 mL) in PBS in the sample tube was placed in a degasified water bath at 20 or 42 °C. The ultrasound images and videos were simultaneously recorded (B mode, Philips IU22, with the MI of 0.8). The gray value of ultrasound imaging was calculated by software.

To evaluate the US imaging ability of PFP bubbles, PBS, solutions of HPB-PFP (100 ppm, 3 mL) and HPB (100 ppm, 3 mL) in the sample tube were placed in a degasification water bath at 42 °C concurrently. The US images and videos were simultaneously recorded (B mode, Philips IU22, with the MI of 0.8). The gray value of ultrasound imaging was recorded using software.

In Vivo Ultrasound Imaging with HPB-PFP. Animal experiments in the present study were in accordance with the policies of National Ministry of Health and were performed according to protocols approved by the Tongji University Laboratory Animal Center. The tumor model was constructed by subcutaneous injection of 100 μL of serum-free DMEM culture medium containing 1 × 10^6 HeLa cells into the back of Balb/c nude mouse (female, 4 weeks old, with the body weight of ~20 g). When the tumor nodule attained a diameter of ~0.8 cm, the mouse was anaesthetized and an US image of the tumor was taken under the B mode with IU22 (with MI of 0.8). Then, 30 μL of HPB-PFP solution (200 ppm, in PBS) was

DOI: 10.1021/am507443p
ACS Appl. Mater. Interfaces 2015, 7, 4579−4588

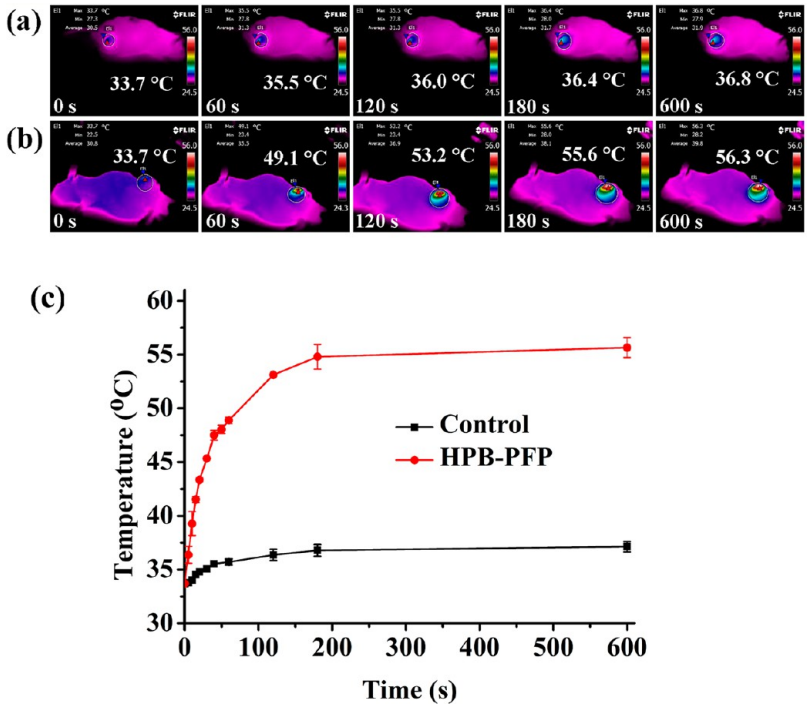

Figure 4. Thermal infrared camera photos of (a) control and (b) treatment group at different time after irradiation. (c) Temperature-change curves of tumors in each group during 10 min of irradiation.

intratumorally injected and the US image of the tumor was immediately recorded using IU22 (MI = 0.8). To observe the influence of PFP bubbles on the US image, the mouse with intratumorally HPB-PFP injection was then irradiated with 808 nm laser light at 2 W/cm^2 for 5 min, followed by US imaging using IU22 (MI = 0.8). The gray values of all ultrasound imaging were recorded by software.

In Vivo Thermal Treatment. Twelve tumor-bearing Balb/c nude mice were randomly divided into two groups (n = 6 per group). Then, 30 μL of saline or HPB-PFP (200 ppm) dispersed into saline was intratumorally injected into each mouse, and the tumor was irradiated with 808 nm laser light at 2 W/cm^2 for 10 min. The average tumor temperature was monitored using a thermal infrared camera (FLIR T420). Relative tumor volume (V/V_0 where V_0 represents the initial (i.e., day 0) tumor volume of each mouse) and tumor appearance were monitored at different time points.

Western Blot and TUNEL Staining. Tumors in control and treatment groups were harvested at 30 min post PTT. Western blot analysis was carried out to detect the expression of p53, Bcl-2, Bax, ß-actin, and their cleaved fractions in total protein and Cyto C in cytosolic protein. TdT-mediated dUTP nick-end labeling (TUNEL) staining of tumor tissues was measured to further observe the appearance of tumor cells after PTT.

Pathological Analysis of Animal Main Organs. Twenty-eight Kunming mice (~25 g) were randomly divided into four groups (n = 7 per group). HPB in PBS (3 mg/mL, 0.2 mL) was intravenously injected into the mice. Mice injected with PBS were set as control. At 7, 30, and 60 d post injection, the mice were euthanized, and organs (heart, liver, lung, spleen, and kidney) were collected to stain with hematoxylin and eosin for analysis of tissue pathological changes.

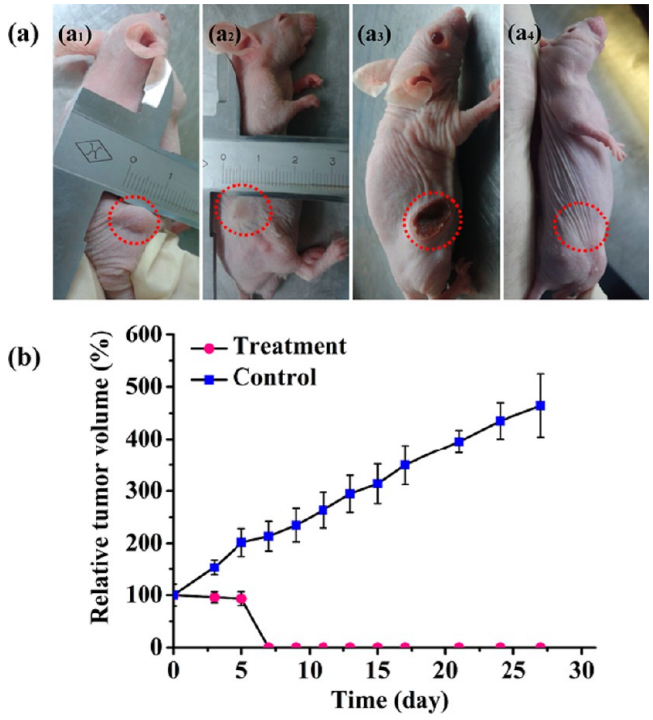

Figure 5. (a) Digital photos of the nude mouse tumor (red dotted circle) in the whole therapeutic process (a_1, before therapy; a_2, after laser irradiation; a_3, second day after laser irradiation; a_4, one month after laser irradiation). (b) Relative tumor volume with time after PTT curve.

RESULTS AND DISCUSSIONS

Synthesis and Characterization of HPB. PVP molecules have been intensively used during the synthesis of nanomaterials because the surface-anchored PVP can improve the biological and immunological compatibility.[56,57] As shown in Figure 1a, mPB NPs with a uniform size of about 500 nm are successfully prepared. Electron diffraction imaging reveals that the mPB nanocubes have a single-crystal structure (inset of Figure 1a). To create a hollow structure within mPB, mPB nanocubes were etched by the solution of HCl with the assistance of hydrothermal treatment for 4 h at 140 °C. After HCl etching, HPB NPs with a large number of cavities were

DOI: 10.1021/am507443p
ACS Appl. Mater. Interfaces 2015, 7, 4579−4588

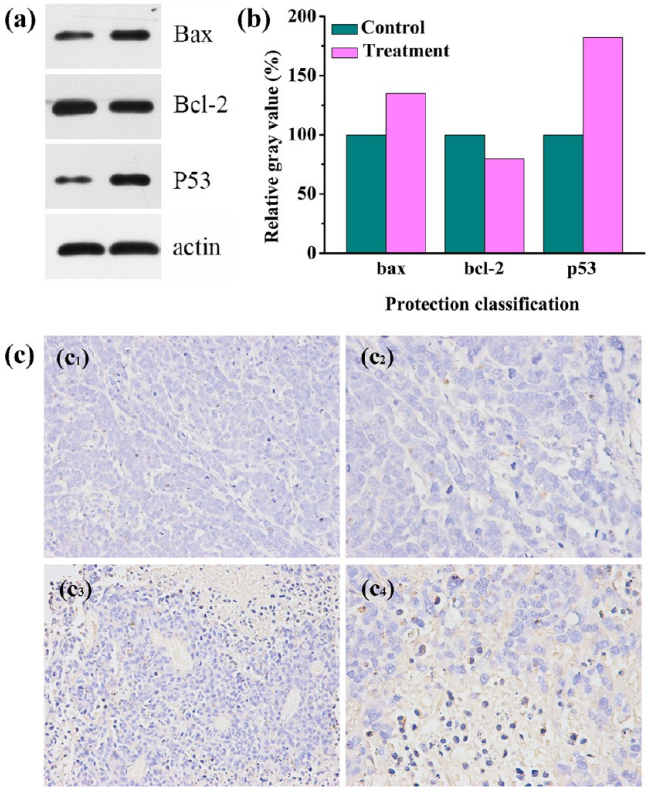

Figure 6. (a) Western blot of mice tumors under different treatment for demonstrating in vivo cell necrosis. (b) Relative gray values corresponding to Western blot. (c) TUNEL staining images of tumors in the two groups (c_1 and c_2, control group; c_3 and c_4, treatment group; c_1 and c_3, 200 fold; c_2 and c_4, 400 fold).

formed (Figure 1b–e). In particular, the HPB can keep the single-crystal structure (Figure 1c inset). The elemental mapping of C, N, and Fe in HPB demonstrates the uniform distribution of these chemical elements in the whole HPB NPs (Figure 1e–i). The energy dispersive spectrum (EDS) of HPB confirms the existence of C, N, and Fe elements (Figure S1 in the Supporting Information), and the prepared HPB NPs can be well-dispersed in both water and PBS with high stability (inset of Figure 1b).

ζ potentials and hydrated ionic diameters of mPB and HPB were measured for comparison by dynamic light scattering (DLS) (Figure S2 in the Supporting Information). The HPB NPs show ζ potential (−20 mV) and particle-size distribution that are the same as those of mPB in deionized water (Figure S2a,b in the Supporting Information), indicating that the chemical composition and surface characteristics of mPB did not make obvious changes during the etching process. The UV–vis–NIR absorption spectra of different concentrations of HPB in PBS (12.5, 25, 50, 100, and 200 ppm) show a broad absorption and a strong absorption peak at about 710 nm, and a slight blue shift occurs with the increase of HPB concentration (Figure S3 in the Supporting Information).

As shown in Figure 2a (2.5 W/cm^2) and Figure 2b (5 W/cm^2), the PBS temperature shows a little increase with the increase of the power density of the laser, while the temperature of HPB suspension has obviously increased with the laser power density at different concentrations (25, 50, 100, and 200 ppm). The solution temperature increase about 15 °C (Figure 2a) at 2.5 W/cm^2 and 35 °C (Figure 2b) at 5 W/cm^2 after 10 min of irradiation with the HPB concentration of 200 ppm. Furthermore, HPB-PFP shows almost the same photothermal translation efficiency with HPB (Figure S4 in the Supporting Information), indicating that PFP inside cannot affect the photosensitizing ability of HPB. The continuous temperature elevation demonstrates that HPB NPs have a high

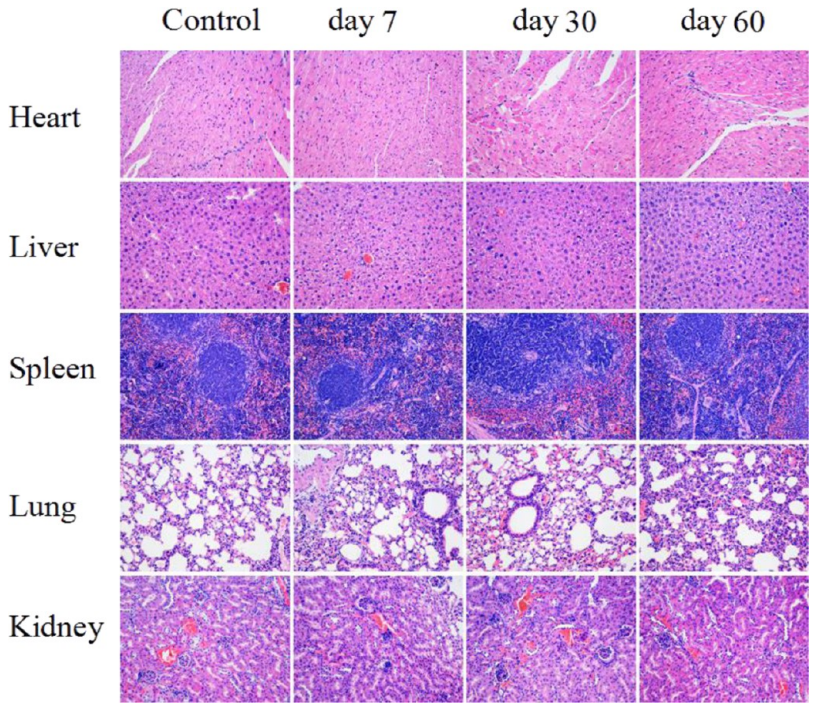

Figure 7. Histological examinations of major organs (heart, liver, spleen, lung, and kidney) after injection of HPB in different periods of time (7, 30, and 60 days).

DOI: 10.1021/am507443p
ACS Appl. Mater. Interfaces 2015, 7, 4579–4588

molar extinction coefficient and can absorb the NIR light to efficiently translate it into heat. This characteristic can be ascribed to the energy change caused by the NIR photon-mediated charge transition between Fe^{2+} and Fe^{3+} ions in HPB.[55]

In Vitro Photothermal Effect. To demonstrate biocompatibility of HPB, HeLa cells were cultured with HPB (0, 50, 100, 200, and 400 ppm) for 24 and 48 h. Quantitative results from MTT assay are shown in Figure S5 in the Supporting Information. No significant cytotoxicity was observed after a 24 or 48 h incubation of cells with different concentrations of HPB. The in vitro PTT efficiency of HPB against cancer cells was further investigated by using the quantitative MTT assay, with the irradiation of NIR. As shown in Figure 2c, after coincubation with HPB and exposure to 808 nm laser light (5 W/cm^2) for 5 min, HeLa cells show a concentration-dependent cell death, clearly implying the HPB NPs after being injected into tumor can efficiently absorb and transform the NIR laser light into heat, resulting in significant killing of cancer cells. CLSM was further used to directly observe the apoptosis and necrosis of cells caused by the heating effect of HPB after absorbing NIR light. Calcein can pass through cell membranes and dye the living cells, whereas PI, as a nucleus dye, can pass through only nonviable cell-cracked membranes. Thus, living cells display a green florescence while nonviable cells exhibit red under CLSM. As shown in Figure 2d, plenty of green living cells (Figure 2d$_1$) with few apoptotic and/or necrotic cells (Figure 2d$_2$) in the control can be detected from CLSM images. After being irradiated with NIR laser light at 5 W/cm^2 for 5 min, an increasing area of red stained cells (Figure 2d$_3$,d$_4$) can be observed. More obvious regions of destroyed cells (showing red) are observed after 10 min of laser irradiation (Figure 2d$_5$,d$_6$), further implying that HPB can efficiently absorb and transform NIR laser light into heat and efficiently burn and kill tumor cells.

Enhanced Ultrasound Imaging with HPB-PFP. The inside hollow structure of HPB encourages us to employ it as a US contrast agent to realize the real-time monitoring of the tumor by US imaging. The thermosensitive PFP with an excellent biosafety and low boiling point (29.2 °C) was chosen as guest molecule to encapsulate into HPB. As a highly volatile liquid, PFP can be gasified considerably upon heating. The outer shell of HPB can convert NIR light energy into heat to induce the liquid−gas phase change of PFP. No bubble could be detected when PBS (right-hand panel of Figure 3a and Figure 3b$_1$, movie 1 of Supporting Information) and HPB solution without PFP (middle panel of Figure 3a) were used as the US contrast, even though the temperature was set at 42 °C, confirming that the observed change in US imaging contrast arises mainly from PFP release and HPB will not affect the in vivo US imaging signal. For the HPB-PFP solution, only a few bubbles went up at 20 °C (Figure 3b$_2$, movie 2 of Supporting Information), whereas abundant PFP bubbles appeared instantly, implying the PFP is boiling, at 42 °C (Figure 3b$_3$, movie 3 of Supporting Information), which convincingly demonstrated the excellent in vitro photoactivated ultrasound-imaging effect of HPB-PFP. The quantitative gray values of PBS and HPB-PFP suspension further show the obviously enhanced US imaging outcome caused by the PFP phase change (Figure 3d).

The in vivo ultrasound-imaging performance of HPB-PFP against tumor-bearing mice was further conducted under B mode with IU22 (with the MI of 0.8). The ultrasound images of the subcutaneously transplanted HeLa tumor tissue were captured before and after intratumor injection of HPB-PFP. The tumor tissue presents a dark image before injection (control, Figure 3c$_1$) and then becomes a little bit bright after injection of HPB-PFP (Figure 3c$_2$) because of the accumulation of HPB-PFP NPs. Importantly, greatly enhanced ultrasound signal can be observed after tumor tissue was irradiated by the NIR laser light for 5 min (Figure 3c$_3$). The significant enhancement of ultrasound signal can be attributed to the gasification of PFP when the HPB shell converted the absorbed light into heat. The generated PFP microbubbles caused the tissue impedance mismatch and reflected the ultrasound beam to enhance the echogenicity signal. The quantitative gray value of tumor sites shows a more than 10-fold increase after the tumor received the laser irradiation (Figure 3e), further indicative of the obvious enhancement of US imaging; thus, the as-prepared HPB-PFP is expected to be used for US imaging contrast to guide the PTT of cancer.

In Vivo Effect of Thermal Treatment. Encouraged by the excellent in vitro PTT effect of HPB, we further investigated the in vivo PTT efficiency against HeLa xenograft bearing Balb/c nude mice. Panels a and b of Figure 4 show the tumor temperature change of the mouse without and with HPB injection, respectively. For the tumor injected with HPB-PFP and irradiated with 808 nm laser light at 2 W/cm^2 for 10 min, the temperature of tumor sites rise quickly from initial 33.7 to 49.1 °C within the first 60 s (Figure 4b). This can be attributed to the fact that HPB-PFP can absorb NIR light and translate it into heat efficiently, thus causing the swift increase of tumor temperature. The temperature reached 56.3 °C after 10 min of irradiation. In sharp contrast, the tumor temperature in the control group shows only a slight increase of about 3 °C even after 10 min of exposure (Figure 4a). The temperature change of tumors is plotted in Figure 4c to better illustrate the photothermal transform efficiency of HPB-PFP. Apparently, HPB-PFP shows an excellent in vivo photothermal transformation performance. To further evaluate the long-term in vivo PTT therapeutic efficiency, the tumor volumes were monitored every 2 days for 4 weeks. The tumor growth could be significantly inhibited in PTT treatment group (Figure 5b). After laser irradiation, the volume of the tumor was below 90% in 5 days of continued feeding. The ablation scars were sloughed away and almost completely disappeared after 1 week. More excitingly, the tumor recurrence could not be observed in the following 28 days of feeding. Figure 5a$_4$ shows the ultimate healed skin of the treatment group mouse. For comparison, the continuous increase of tumor volume can be found in the control group, i.e., the tumor volume of the control group increased by 200% in the fifth day and close to 500% in one month (Figure 5b). Such ideal photothermal therapeutic results demonstrate that HPB-PFP can eradicate the tumor and will be as an admirable PTT agent in the future.

TUNEL immunostaining of tumor tissues shows that the PTT process induces a large number of cell apoptosis and necrosis, more nucleus contraction, and cell morphology destruction (Figure 6c$_3$,c$_4$), whereas cells apoptosis and necrosis are hardly to be found in the control group (Figure 6c$_1$,c$_2$). The pathological results of tumor tissue demonstrate the occurrence of cell apoptosis caused by the heating effect. Cell apoptosis is the main form of programmed cell death regulated by various genes. To further investigate the relevant factors of tumor cell apoptosis after thermal ablation treatment,

DOI: 10.1021/am507443p
ACS Appl. Mater. Interfaces 2015, 7, 4579−4588

western blot analysis of Bcl-2 family and p53 proteins, collected from the tumor cells of the two groups with and without thermal therapy, respectively, have been conducted (Figure 6a). The greatly increased gray value of p53 protein expression can be attributed to the promotion mechanism of cell apoptosis (Figure 6b). Mice treated with HPB-PFP and NIR laser light show more apoptosis, as evidenced by the overexpression of Bax protein and low expression of Bcl-2 protein (as shown in Figure 6b). All the results obviously demonstrate that heat can cause over or low expression of the genes and proteins, thus facilitating the destruction of tumor tissues.

Finally, to further illustrate the excellent biocompatibility of HPB in vivo, long-term toxicity toward major organs including heart, liver, spleen, lung, and kidney has been evaluated using HE staining in different periods of time (7 days, 1 month, 2 months), after the intravenous injection of HPB solution (200 μL, 3 mg/mL) into mice. There are no obvious histological alteration or injury in cellular structures between the organs of the HPB-injected mice and untreated mice (Figure 7). Therefore, HPB-PFP shows promise for use as an ideal PTT agent and US imaging contrast agent for further clinical medicine.

CONCLUSION

A novel photothermal conversion agent HPB with hollow mesoporous structure was prepared via a facile and efficient chemical-etching method assisted by hydrochloric acid. The hydrophobic perfluorocarbon compound was encapsulated into HPB through a vacuuming procedure for US imaging-guided PTT. The HPB NPs exhibited high dispersity, large cavity, well-defined mesoporosity, and high biocompatibility. Importantly, HPB could absorb 808 nm laser light and efficiently transform it into heat to destroy tumors both in vitro and in vivo. In addition, the heat translated by HPB could cause the liquid–gas phase transition of thermosensitive PFP with low boiling point for substantial ultrasound imaging enhancement. The demonstration of light-activated phase-changing for concurrent ultrasound imaging and PTT against cancer cells show the great potential for imaging-guided cancer therapy.

ASSOCIATED CONTENT

Supporting Information

Additional material characterization, HeLa cell relative viabilities, US imaging and movies of bubble formation data. This material is available free of charge via the Internet at http://pubs.acs.org.

AUTHOR INFORMATION

Corresponding Authors

*E-mail: hrchen@mail.sic.ac.cn.
*E-mail: wuhuixia@shnu.edu.cn.

Author Contributions

$^{\perp}$X.J. and X.C. contributed equally to this work.

Notes

The authors declare no competing financial interest.

ACKNOWLEDGMENTS

This work was supported by the National Basic Research Program of China (973 Program, Grant 2011CB707905), China National Funds for Distinguished Young Scientists (51225202), National Natural Science Foundation of China (Grant 51132009), Program of Shanghai Subject Chief Scientist (Grant 14XD1403800), and the Shanghai Municipal Education Commission (14ZZ128).

REFERENCES

(1) Hu, M.; Furukawa, S.; Ohtani, R.; Sukegawa, H.; Nemoto, Y.; Reboul, J.; Kitagawa, S.; Yamauchi, Y. Synthesis of Prussian Blue Nanoparticles with a Hollow Interior by Controlled Chemical Etching. *Angew. Chem., Int. Ed.* **2011**, *51*, 984–988.

(2) Hu, M.; Torad, N. L.; Yamauchi, Y. Preparation of Various Prussian Blue Analogue Hollow Nanocubes with Single Crystalline Shells. *Eur. J. Inorg. Chem.* **2012**, *2012*, 4795–4799.

(3) Kandanapitiye, M. S.; Valley, B.; Yang, L. D.; Fry, A. M.; Woodward, P. M.; Huang, S. D. Gallium Analogue of Soluble Prussian Blue KGa[Fe(CN)$_6$]·nH$_2$O: Synthesis, Characterization, and Potential Biomedical Applications. *Inorg. Chem.* **2013**, *52*, 2790–2792.

(4) Shokouhimehr, M.; Soehnlen, E. S.; Khitrin, A.; Basu, S.; Huang, S. D. Biocompatible Prussian Blue Nanoparticles: Preparation, Stability, Cytotoxicity, and Potential Use as an MRI Contrast Agent. *Inorg. Chem. Commun.* **2009**, *13*, 58–61.

(5) Uemura, T.; Ohba, M.; Kitagawa, S. Size and Surface Effects of Prussian Blue Nanoparticles Protected by Organic Polymers. *Inorg. Chem.* **2004**, *43*, 7339–7345.

(6) Pintado, S.; Goberna-Ferrón, S.; Escudero-Adán, E. C.; Galán-Mascarós, J. R. Fast and Persistent Electrocatalytic Water Oxidation by Co–Fe Prussian Blue Coordination Polymers. *J. Am. Chem. Soc.* **2013**, *135*, 13270–13273.

(7) Qian, L.; Zheng, R.; Zheng, L. Fabrication of Prussian Blue Nanocubes through Reducing a Single-Source Precursor with Graphene Oxide and Their Electrocatalytic Activity for H_2O_2. *J. Nanopart. Res.* **2013**, *15*, 1–9.

(8) Wang, H.; Huang, Y. Prussian-Blue-Modified Iron Oxide Magnetic Nanoparticles as Effective Peroxidase-like Catalysts to Degrade Methylene Blue with H_2O_2. *J. Hazard. Mater.* **2011**, *191*, 163–169.

(9) Yuqing, M.; Jiwei, L. Assembly and Electroanalytical Performance of Prussian Blue/polypyrrole Composite Nanoparticles Synthesized by the Reverse Micelle Method. *Sci. Technol. Adv. Mater.* **2009**, *10*, 025001.

(10) Shokouhimehr, M.; Soehnlen, E. S.; Hao, J.; Griswold, M.; Flask, C.; Fan, X.; Basilion, J. P.; Basu, S.; Huang, S. D. Dual Purpose Prussian Blue Nanoparticles for Cellular Imaging and Drug Delivery: A New Generation of T_1-weighted MRI Contrast and Small Molecule Delivery Agents. *J. Mater. Chem.* **2010**, *20*, 5251–5259.

(11) Liang, X.; Deng, Z.; Jing, L.; Li, X.; Dai, Z.; Li, C.; Huang, M. Prussian Blue Nanoparticles Operate as a Contrast Agent for Enhanced Photoacoustic Imaging. *Chem. Commun. (Cambridge, U.K.)* **2013**, *49*, 11029–11031.

(12) Perrier, M.; Kenouche, S.; Long, J.; Thangavel, K.; Larionova, J.; Goze-Bac, C.; Lascialfari, A.; Mariani, M.; Baril, N.; Guérin, C.; Donnadieu, B.; Trifonov, A.; Guari, Y. Investigation on NMR Relaxivity of Nano-Sized Cyano-Bridged Coordination Polymers. *Inorg. Chem.* **2013**, *52*, 13402–13414.

(13) Shao-Jen, W.; Chun-Sheng, C.; Lin-Chi, C. Prussian Blue Nanoparticles as Nanocargoes for Delivering DNA Drugs to Cancer Cells. *Sci. Technol. Adv. Mater.* **2013**, *14*, 044405.

(14) Fu, G.; Liu, W.; Feng, S.; Yue, X. Prussian Blue Nanoparticles Operate as a New Generation of Photothermal Ablation Agents for Cancer Therapy. *Chem. Commun. (Cambridge, U.K.)* **2012**, *48*, 11567–11569.

(15) Lian, H.-Y.; Hu, M.; Liu, C.-H.; Yamauchi, Y.; Wu, K. C.-W. Highly Biocompatible, Hollow Coordination Polymer Nanoparticles as Cisplatin Carriers for Efficient Intracellular Drug Delivery. *Chem. Commun. (Cambridge, U.K.)* **2012**, *48*, 5151–5153.

(16) Gong, H.; Dong, Z.; Liu, Y.; Yin, S.; Cheng, L.; Xi, W.; Xiang, J.; Liu, K.; Li, Y.; Liu, Z. Engineering of Multifunctional Nano-Micelles for Combined Photothermal and Photodynamic Therapy Under the Guidance of Multimodal Imaging. *Adv. Funct. Mater.* **2014**, *24*, 6492–6502.

DOI: 10.1021/am507443p
ACS Appl. Mater. Interfaces 2015, 7, 4579–4588

(17) Huang, P.; Rong, P.; Jin, A.; Yan, X.; Zhang, M. G.; Lin, J.; Hu, H.; Wang, Z.; Yue, X.; Li, W.; Niu, G.; Zeng, W.; Wang, W.; Zhou, K.; Chen, X. Dye-Loaded Ferritin Nanocages for Multimodal Imaging and Photothermal Therapy. *Adv. Mater. (Weinheim, Ger.)* **2014**, *24*, 6401−6408.
(18) Liu, T.; Wang, C.; Gu, X.; Gong, H.; Cheng, L.; Shi, X.; Feng, L.; Sun, B.; Liu, Z. Drug Delivery with PEGylated MoS_2 Nano-Sheets for Combined Photothermal and Chemotherapy of Cancer. *Adv. Mater. (Weinheim, Ger.)* **2013**, *26*, 3433−3440.
(19) Xiao, Q.; Zheng, X.; Bu, W.; Ge, W.; Zhang, S.; Chen, F.; Xing, H.; Ren, Q.; Fan, W.; Zhao, K.; Hua, Y.; Shi, J. A Core/Satellite Multifunctional Nanotheranostic for in Vivo Imaging and Tumor Eradication by Radiation/Photothermal Synergistic Therapy. *J. Am. Chem. Soc.* **2013**, *135*, 13041−13048.
(20) Wu, X.; Ming, T.; Wang, X.; Wang, P.; Wang, J.; Chen, J. High-Photoluminescence-Yield Gold Nanocubes: For Cell Imaging and Photothermal Therapy. *ACS Nano* **2010**, *4*, 113−120.
(21) Ayala-Orozco, C.; Urban, C.; Knight, M. W.; Urban, A. S.; Neumann, O.; Bishnoi, S. W.; Mukherjee, S.; Goodman, A. M.; Charron, H.; Mitchell, T.; Shea, M.; Roy, R.; Nanda, S.; Schiff, R.; Halas, N. J.; Joshi, A. Au Nanomatryoshkas as Efficient Near-Infrared Photothermal Transducers for Cancer Treatment: Benchmarking against Nanoshells. *ACS Nano* **2014**, *8*, 6372−6381.
(22) Choi, W. I.; Kim, J.-Y.; Kang, C.; Byeon, C. C.; Kim, Y. H.; Tae, G. Tumor Regression *In Vivo* by Photothermal Therapy Based on Gold-Nanorod-Loaded, Functional Nanocarriers. *ACS Nano* **2011**, *5*, 1995−2003.
(23) Huang, X.; El-Sayed, I. H.; Qian, W.; El-Sayed, M. A. Cancer Cell Imaging and Photothermal Therapy in the Near-Infrared Region by Using Gold Nanorods. *J. Am. Chem. Soc.* **2006**, *128*, 2115−2120.
(24) Tsai, M.-F.; Chang, S.-H. G.; Cheng, F.-Y.; Shanmugam, V.; Cheng, Y.-S.; Su, C.-H.; Yeh, C.-S. Au Nanorod Design as Light-Absorber in the First and Second Biological Near-Infrared Windows for in Vivo Photothermal Therapy. *ACS Nano* **2013**, *7*, 5330−5342.
(25) Chen, Y.; Xu, P.; Shu, Z.; Wu, M.; Wang, L.; Zhang, S.; Zheng, Y.; Chen, H.; Wang, J.; Li, Y.; Shi, J. Multifunctional Graphene Oxide-based Triple Stimuli-Responsive Nanotheranostics. *Adv. Funct. Mater.* **2014**, *24*, 4386−4396.
(26) Hu, S.-H.; Chen, Y.-W.; Hung, W.-T.; Chen, I. W.; Chen, S.-Y. Quantum-Dot-Tagged Reduced Graphene Oxide Nanocomposites for Bright Fluorescence Bioimaging and Photothermal Therapy Monitored in Situ. *Adv. Mater. (Weinheim, Ger.)* **2011**, *24*, 1748−1754.
(27) Jung, H. S.; Kong, W. H.; Sung, D. K.; Lee, M.-Y.; Beack, S. E.; Keum, D. H.; Kim, K. S.; Yun, S. H.; Hahn, S. K. Nanographene Oxide−Hyaluronic Acid Conjugate for Photothermal Ablation Therapy of Skin Cancer. *ACS Nano* **2014**, *8*, 260−268.
(28) Liang, C.; Diao, S.; Wang, C.; Gong, H.; Liu, T.; Hong, G.; Shi, X.; Dai, H.; Liu, Z. Tumor Metastasis Inhibition by Imaging-Guided Photothermal Therapy with Single-Walled Carbon Nanotubes. *Adv. Mater. (Weinheim, Ger.)* **2014**, *26*, 5646−5652.
(29) Robinson, J. T.; Tabakman, S. M.; Liang, Y.; Wang, H.; Sanchez Casalongue, H.; Vinh, D.; Dai, H. Ultrasmall Reduced Graphene Oxide with High Near-Infrared Absorbance for Photothermal Therapy. *J. Am. Chem. Soc.* **2011**, *133*, 6825−6831.
(30) Wang, Y.; Wang, K.; Zhang, R.; Liu, X.; Yan, X.; Wang, J.; Wagner, E.; Huang, R. Synthesis of Core-Shell Graphitic Carbon@ Silica Nanospheres with Dual-Ordered Mesopores for Cancer-Targeted Photothermochemotherapy. *ACS Nano* **2014**, *8*, 7870−7879.
(31) Wang, Y.; Wang, K.; Zhao, J.; Liu, X.; Bu, J.; Yan, X.; Huang, R. Multifunctional Mesoporous Silica-Coated Graphene Nanosheet Used for Chemo-Photothermal Synergistic Targeted Therapy of Glioma. *J. Am. Chem. Soc.* **2013**, *135*, 4799−4804.
(32) Dong, K.; Liu, Z.; Li, Z.; Ren, J.; Qu, X. Hydrophobic Anticancer Drug Delivery by a 980 nm Laser-Driven Photothermal Vehicle for Efficient Synergistic Therapy of Cancer Cells in Vivo. *Adv. Mater. (Weinheim, Ger.)* **2013**, *25*, 4452−4458.
(33) Guo, L.; Yan, D. D.; Yang, D.; Li, Y.; Wang, X.; Zalewski, O.; Yan, B.; Lu, W. Combinatorial Photothermal and Immuno Cancer Therapy Using Chitosan-Coated Hollow Copper Sulfide Nanoparticles. *ACS Nano* **2014**, *8*, 5670−5681.
(34) Liu, X.; Wang, X.; Swihart, M. T. $Cu_{2-x}S_{1-y}Se_y$ Alloy Nanocrystals with Broadly Tunable Near-Infrared Localized Surface Plasmon Resonance. *Chem. Mater.* **2013**, *25*, 4402−4408.
(35) Xie, Y.; Riedinger, A.; Prato, M.; Casu, A.; Genovese, A.; Guardia, P.; Sottini, S.; Sangregorio, C.; Miszta, K.; Ghosh, S.; Pellegrino, T.; Manna, L. Copper Sulfide Nanocrystals with Tunable Composition by Reduction of Covellite Nanocrystals with Cu^+ Ions. *J. Am. Chem. Soc.* **2013**, *135*, 17630−17637.
(36) Yu, X. L.; Cao, C. B.; Zhu, H. S.; Li, Q. S.; Liu, C. L.; Gong, Q. H. Nanometer-Sized Copper Sulfide Hollow Spheres with Strong Optical-Limiting Properties. *Adv. Funct. Mater.* **2007**, *17*, 1397−1401.
(37) Zhou, M.; Zhang, R.; Huang, M.; Lu, W.; Song, S.; Melancon, M. P.; Tian, M.; Liang, D.; Li, C. A Chelator-Free Multifunctional [^{64}Cu]CuS Nanoparticle Platform for Simultaneous Micro-PET/CT Imaging and Photothermal Ablation Therapy. *J. Am. Chem. Soc.* **2010**, *132*, 15351−15358.
(38) Chen, Z.; Wang, Q.; Wang, H.; Zhang, L.; Song, G.; Song, L.; Hu, J.; Wang, H.; Liu, J.; Zhu, M.; Zhao, D. Ultrathin PEGylated $W_{18}O_{49}$ Nanowires as a New 980 nm-Laser-Driven Photothermal Agent for Efficient Ablation of Cancer Cells In Vivo. *Adv. Mater. (Weinheim, Ger.)* **2012**, *25*, 2095−2100.
(39) Cheng, L.; Liu, J.; Gu, X.; Gong, H.; Shi, X.; Liu, T.; Wang, C.; Wang, X.; Liu, G.; Xing, H.; Bu, W.; Sun, B.; Liu, Z. PEGylated WS_2 Nanosheets as a Multifunctional Theranostic Agent for in vivo Dual-Modal CT/Photoacoustic Imaging Guided Photothermal Therapy. *Adv. Mater. (Weinheim, Ger.)* **2013**, *26*, 1886−1893.
(40) Guo, C.; Yin, S.; Yan, M.; Kobayashi, M.; Kakihana, M.; Sato, T. Morphology-Controlled Synthesis of $W_{18}O_{49}$ Nanostructures and Their Near-Infrared Absorption Properties. *Inorg. Chem.* **2012**, *51*, 4763−4771.
(41) Kalluru, P.; Vankayala, R.; Chiang, C.-S.; Hwang, K. C. Photosensitization of Singlet Oxygen and in Vivo Photodynamic Therapeutic Effects Mediated by PEGylated $W_{18}O_{49}$ Nanowires. *Angew. Chem., Int. Ed.* **2013**, *52*, 12332−12336.
(42) Liu, Y.; Ai, K.; Liu, J.; Deng, M.; He, Y.; Lu, L. Dopamine-Melanin Colloidal Nanospheres: An Efficient Near-Infrared Photothermal Therapeutic Agent for In Vivo Cancer Therapy. *Adv. Mater. (Weinheim, Ger.)* **2012**, *25*, 1353−1359.
(43) Wang, C.; Xu, H.; Liang, C.; Liu, Y.; Li, Z.; Yang, G.; Cheng, L.; Li, Y.; Liu, Z. Iron Oxide @ Polypyrrole Nanoparticles as a Multifunctional Drug Carrier for Remotely Controlled Cancer Therapy with Synergistic Antitumor Effect. *ACS Nano* **2013**, *7*, 6782−6795.
(44) Zha, Z.; Yue, X.; Ren, Q.; Dai, Z. Uniform Polypyrrole Nanoparticles with High Photothermal Conversion Efficiency for Photothermal Ablation of Cancer Cells. *Adv. Mater. (Weinheim, Ger.)* **2013**, *25*, 777−782.
(45) Tranquart, F.; Grenier, N.; Eder, V.; Pourcelot, L. Clinical Use of Ultrasound Tissue Harmonic Imaging. *Ultrasound Med. Biol.* **1999**, *25*, 889−894.
(46) Hannah, A.; Luke, G.; Wilson, K.; Homan, K.; Emelianov, S. Indocyanine Green-Loaded Photoacoustic Nanodroplets: Dual Contrast Nanoconstructs for Enhanced Photoacoustic and Ultrasound Imaging. *ACS Nano* **2014**, *8*, 250−259.
(47) Sheeran, P. S.; Luois, S. H.; Mullin, L. B.; Matsunaga, T. O.; Dayton, P. A. Design of Ultrasonically-Activatable Nanoparticles Using Low Boiling Point Perfluorocarbons. *Biomaterials* **2012**, *33*, 3262−3269.
(48) Zhou, Y.; Wang, Z.; Chen, Y.; Shen, H.; Luo, Z.; Li, A.; Wang, Q.; Ran, H.; Li, P.; Song, W.; Yang, Z.; Chen, H.; Wang, Z.; Lu, G.; Zheng, Y. Microbubbles from Gas-Generating Perfluorohexane Nanoemulsions for Targeted Temperature-Sensitive Ultrasonography and Synergistic HIFU Ablation of Tumors. *Adv. Mater. (Weinheim, Ger.)* **2013**, *25*, 4123−4130.
(49) Chung, M.-F.; Chen, K.-J.; Liang, H.-F.; Liao, Z.-X.; Chia, W.-T.; Xia, Y.; Sung, H.-W. A Liposomal System Capable of Generating

DOI: 10.1021/am507443p
ACS Appl. Mater. Interfaces 2015, 7, 4579−4588

CO_2 Bubbles to Induce Transient Cavitation, Lysosomal Rupturing, and Cell Necrosis. *Angew. Chem., Int. Ed.* **2012**, *51*, 10089−10093.
(50) Nakatsuka, M. A.; Mattrey, R. F.; Esener, S. C.; Cha, J. N.; Goodwin, A. P. Aptamer-Crosslinked Microbubbles: Smart Contrast Agents for Thrombin-Activated Ultrasound Imaging. *Adv. Mater. (Weinheim, Ger.)* **2012**, *24*, 6010−6016.
(51) Huynh, E.; Lovell, J. F.; Helfield, B. L.; Jeon, M.; Kim, C.; Goertz, D. E.; Wilson, B. C.; Zheng, G. Porphyrin Shell Microbubbles with Intrinsic Ultrasound and Photoacoustic Properties. *J. Am. Chem. Soc.* **2012**, *134*, 16464−16467.
(52) Moon, G. D.; Choi, S.-W.; Cai, X.; Li, W.; Cho, E. C.; Jeong, U.; Wang, L. V.; Xia, Y. A New Theranostic System Based on Gold Nanocages and Phase-Change Materials with Unique Features for Photoacoustic Imaging and Controlled Release. *J. Am. Chem. Soc.* **2011**, *133*, 4762−4765.
(53) Chen, Y.; Yin, Q.; Ji, X.; Zhang, S.; Chen, H.; Zheng, Y.; Sun, Y.; Qu, H.; Wang, Z.; Li, Y.; Wang, X.; Zhang, K.; Zhang, L.; Shi, J. Manganese Oxide-Based Multifunctionalized Mesoporous Silica Nanoparticles for pH-Responsive MRI, Ultrasonography and Circumvention of MDR in Cancer Cells. *Biomaterials* **2012**, *33*, 7126−7137.
(54) Liberman, A.; Wu, Z.; Barback, C. V.; Viveros, R.; Blair, S. L.; Ellies, L. G.; Vera, D. R.; Mattrey, R. F.; Kummel, A. C.; Trogler, W. C. Color Doppler Ultrasound and Gamma Imaging of Intratumorally Injected 500 nm Iron-Silica Nanoshells. *ACS Nano* **2014**, *7*, 6367−6377.
(55) Fu, G.; Liu, W.; Feng, S.; Yue, X. Prussian Blue Nanoparticles Operate as a New Generation of Photothermal Ablation Agents for Cancer Therapy. *Chem. Commun. (Cambridge, U.K.)* **2012**, *48*, 11567−11569.
(56) Zhi, X.; Fang, H.; Bao, C.; Shen, G.; Zhang, J.; Wang, K.; Guo, S.; Wan, T.; Cui, D. The Immunotoxicity of Graphene Oxides and the Effect of PVP-Coating. *Biomaterials* **2013**, *34*, 5254−5261.
(57) Chen, Y.; Gao, Q.; Wan, H.; Yi, J.; Wei, Y.; Liu, P. Surface Modification and Biocompatible Improvement of Polystyrene Film by Ar, O_2 and Ar + O_2 Plasma. *Appl. Surf. Sci.* **2013**, *265*, 452−457.

DOI: 10.1021/am507443p
ACS Appl. Mater. Interfaces 2015, 7, 4579−4588